

The Nature, Evolution, Clustering and X-ray Properties of Extremely Red Galaxies in the CDFS/GOODS field

Nathan D. Roche^{1,2}, James Dunlop^{1,3}, and Omar Almaini^{1,4}

¹Institute for Astronomy, University of Edinburgh, Royal Observatory, Edinburgh EH9 3HJ, Scotland.

²ndr@roe.ac.uk ³jsd@roe.ac.uk ⁴omar@roe.ac.uk

7 February 2020

ABSTRACT

We identify a deep (to $K_s \sim 22$) sample of extremely red objects (EROs), galaxies with $I - K_s > 3.75$ (numbering 200) or $I - K_s > 4.0$ (163) on 50.4 arcmin^2 of the Chandra Deep Field South, observed as part of the public ESO/GOODS survey.

The ERO number counts attenuate from ~ 0.66 to ~ 0.16 at $K > 19.5$, where they remain well below the predictions for pure luminosity evolution, and fall below even a non-evolving model. This indicates a significant decrease with redshift in the comoving number density of passive/very red galaxies.

We investigate the angular correlation function, $\xi(\theta)$, of these EROs and detect a positive signal at $K_s = 20.5 \pm 2.0$ limits. The $\xi(\theta)$ amplitudes indicate stronger clustering than that of other galaxies at the same magnitudes and are best-fitted by models in which the EROs have a comoving correlation radius $r_0 \sim 11 (12 \text{ h}^{-1} \text{ Mpc})$, or, alternatively, $r_0 \sim 20 (21 \text{ h}^{-1} \text{ Mpc})$ in a stable clustering model.

We find a 40-arcsec diameter grouping of 11 EROs, centered on the Chandra source (and ERO) XID 58, with colours suggesting that at least 7 belong to a cluster of mostly passive EROs at $z \sim 1.5 \pm 1.6$.

The 942 ksec Chandra survey detected 73 X-ray sources in the area of our ERO sample, and we find that 17 of these coincide with EROs. Most of these sources have X-ray properties indicative of obscured AGN, although the faintest 4 may be starbursts or normal ellipticals. In addition, we find evidence that Chandra sources and EROs are positively cross-correlated at non-zero ($\sim 2 \pm 20$ arcsec) separations, implying that they tend to trace the same large-scale structures.

In conclusion these findings appear consistent with a scenario where EROs are the $z > 1$ progenitors of elliptical/S0 galaxies, and evolve from SCUBA sources and high-redshift mergers, via an AGN phase, with some (~ 8 per cent of) EROs being hosts of active, obscured AGN.

Key words: galaxies: evolution; galaxies: elliptical and lenticular, cD; galaxies: high-redshift; X-ray: galaxies

1 INTRODUCTION

The ‘extremely red objects’ (EROs) are a population of very red galaxies (e.g. with $R - K > 5$ or $I - K > 4$) which appear faintward of $K \sim 17.5$. EROs are of special interest in the study of galaxy evolution, in that their colours and other properties suggest that they are the high-redshift ($z \sim 1-2$) counterparts and progenitors of local E/S0 galaxies, and hence include the oldest galaxies present at these redshifts, and may have evolved from the sub-mm galaxies detected with SCUBA at even higher redshifts (e.g. Scott et al. 2002). EROs are more strongly clustered on the sky than other, similarly faint, galaxies (Daddi et al. 2000; Firth et al. 2002), and recent spectroscopy of some of the brightest

EROs (Cimatti et al. 2002; Saracco et al. 2003) has revealed a mixture of old, passive galaxies (hereafter pEROs) and younger star-forming or post-starburst galaxies with strong dusty-reddening (hereafter dsfEROs).

In our previous paper (Roche et al. 2002, hereafter also Paper I), our deep K-band survey of the ELAIS N2’ field with the UFTI (reaching $K \sim 21$) and Ingrid ($K \sim 20$) cameras was combined with a deep R-band image to select a sample of 158 EROs. The number counts of these $R - K > 5.0$ galaxies were lower than predicted by a model in which all E/S0 galaxies evolve by ‘pure luminosity evolution’ (PLE), but could be fitted by a model combining passive luminosity evolution with galaxy merging and a decrease with

redshift in the comoving number density of passive galaxies (merging and negative density evolution').

We measured the clustering of the ERO sample, in the form of the angular correlation function, $\xi(\theta)$. The ERO $\xi(\theta)$ amplitude, combined with those estimated by measurements of Daddi et al. (2000) and Firth et al. (2002), was best-fitted by models with a comoving correlation radius $r_0 \sim 10 \{13 h^{-1} \text{ Mpc}$, which implies the intrinsic clustering of EROs is even stronger than that of present-day $L > L_{\text{ellipticals}} (r_0 \sim 8 h^{-1} \text{ Mpc})$.

We examined the morphology of the 31 brighter ($K < 19.5$) EROs and estimated that ~ 60 per cent were bulge-type galaxies (E/S0s) with the others a mixture of disk, irregular and merging galaxies. The angular sizes of the EROs were generally consistent with our best-fitting evolution model, but inconsistent with a non-evolving model (which underpredicted their surface brightness).

Seven of these 31 brighter EROs were detected as radio sources on a deep VLA survey at 1.4 GHz. One appeared to be a powerful radio galaxy and five were faint point-like radio sources within elliptical galaxies, implying that some

20 per cent of EROs host obscured AGN. The seventh was an elongated radio source, aligned with an extended optical morphology, and probably a dusty starburst galaxy, indicating that some (but only a few per cent) of EROs have star-formation rates as high as the $> 100 \{1000 \text{ M yr}^{-1}$ needed for the starburst to be detected in this VLA survey.

A scenario was proposed in which the pEROs were strongly clustered primordial ellipticals which had formed as SCUBA sources at higher redshifts, whereas the younger dsfEROs were starburst and recent post-starburst galaxies formed from the merging of disk galaxies, which would only later become passive E/S0s. The continual addition of new dsfEROs to the ERO class could then account for both the increase in number and (if dsfEROs are less clustered) dilution of clustering between $z \sim 1 \{2$ EROs and local E/S0s. However, there was a need for these findings to be supported with further and deeper ERO samples.

Recently, Daddi et al. (2002) have claimed that bright ($K < 20$ and $z < 1.5$), spectroscopically selected, pEROs are much more clustered than dsfEROs, although this was based on a small sample in redshift space only, and also needs to be verified.

A further area for investigation concerns the association between EROs and faint X-ray sources. Alexander et al. (2002) and Vignali et al. (2003) found that some of the EROs on the Chandra Deep Field North (CDFN) ($\sim 10 \{30$ per cent depending on magnitude limit) were coincident with X-ray sources in the deep Chandra survey. Secondly, Maini et al. (2002) found that SCUBA sub-mm and Chandra X-ray sources on the ELAIS N2 field, although they rarely coincided, were positively cross-correlated at non-zero separations. This was interpreted as possible evidence for an evolutionary connection, in which the forming giant ellipticals detected as SCUBA sources become X-ray luminous QSOs at the end of the starburst (Archibald et al. 2002). When both starbursting and AGN activity cease, they presumably become red ellipticals, so Chandra sources might show a similar cross-correlation with EROs.

The recent public release of the first installment of the ESO/GOODS survey (with optical and near-infrared imaging of the Chandra Deep Field South (CDFS) (pro-

vided us with an excellent opportunity to investigate the counts and clustering of EROs to a fainter limit than previously, and their association with a very deep sample of X-ray sources.

The layout of this paper is as follows: Section 2 describes the observational data and any data reduction, Section 3 the identification and colour-classification of the EROs, Section 4 the ERO number counts, comparing these with evolutionary models, Section 5 the ERO angular correlation function, $\xi(\theta)$, with an interpretation in terms of intrinsic clustering. In Section 6 we investigate the numbers of close pairs of EROs and identify any larger clusters, in Section 7 the coincidences and correlation between EROs and the Chandra X-ray sources. Section 8 concludes the paper with a discussion of our findings.

In Paper I we had assumed a cosmology with $\Omega_M = 0.3$, $\Omega_\Lambda = 0.7$ (modelled using the analytic form of Pen 1999) and $H_0 = 55 \text{ km s}^{-1} \text{ Mpc}^{-1}$. In view of new results from the Wilkinson Microwave Anisotropy Probe (e.g. Spergel et al. 2003), we here retain this $\Omega_M = 0.3$, but adopt the higher $H_0 = 70 \text{ km s}^{-1} \text{ Mpc}^{-1}$, giving a time since the Big Bang of only 13.48 Gyr. Some H_0 -dependent quantities are given in units of $h = (H_0/100) \text{ km s}^{-1} \text{ Mpc}^{-1}$.

2 OBSERVATIONAL DATA

2.1 Near Infra-red (JHK_s) Imaging

The Great Observatories Origins Deep Survey (GOODS) (Dickinson and Galavisco 2002) is a public, multi-wavelength survey of the Hubble Deep Field North and the Chandra Deep Field South (CDFS). The ESO contribution to GOODS will include deep near-IR and optical imaging of the whole 150 arcmin² of the CDFS. The near-IR observations are being carried out using the ANTU/VLT (Very Large Telescope), with the Infrared Spectrometer and Array Camera (Isaac). ANTU is the first of four 8m instruments, operated by the European Southern Observatory (ESO) at Cerro Paranal, Chile, with the Infrared Spectrometer and Array Camera (Isaac). Isaac is equipped with a Rowell Hawaii 1024 \times 1024 pixel HgCdTe array covering $1 \{2.5 \text{ m}$, with a pixel size 0.1484 arcsec giving a 2.5×2.5 arcminute field-of-view. The CDFS will be covered as a 32-frame mosaic in the J (central = 1.25 m) H (1.65 m) and K_s (2.16 m) passbands.

Isaac observations of the first 8 GOODS fields, covering a contiguous area near the centre of the CDFS, were completed on 1 February 2002 and the data made publicly available on 9 April.

2.2 FORS1 I-band Imaging

Another component of the GOODS survey is deep I-band (I_{BESS} , central = 0.768 m) imaging of the CDFS, again using ANTU, with the Focal Reducer/low dispersion Spectrograph (FORS1). FORS1 is equipped with a 2048 \times 2048 pixel TK 2048EB4-1 CCD, and covers a $6 \{6 \times 6 \text{ arcmin}$ field with pixel size 0.1997 arcsec. The first four pointings on the CDFS, covering a square which includes the full area of the 8 Isaac fields, were publically released on 24 March 2001.

2.3 Chandra X-ray Observations

We also make use of the CDFS X-ray source catalog of Giacconi et al. (2002). The CDFS was observed with the Chandra X-ray Observatory for eleven pointings during 1999{2000, which were combined to give 942 ksec exposure time. On this very deep, high resolution (FWHM \approx 0.7 arcsec) image, Giacconi et al. (2002) detected a total of 346 sources in a soft (0.5{2.0 keV) and/or in a hard (2{10 keV) X-ray band, reaching central-area detection limits $F(0.5\{2.0\text{ keV}) = 5.5 \times 10^{-17}$ and $F(2\{10\text{ keV}) = 4.5 \times 10^{-16}$ erg s⁻¹cm⁻². Of these sources, 73 are on the area of our 8 frames of Isaac data.

3 REDUCTION AND ANALYSIS

3.1 Isaac JH K_s Data

The 8 fields of Isaac data were supplied to us by ESO in a reduced form, as 24 images (8 fields \times 3 passbands) each with a weighting map, astrometry and photometric zero-point. Total exposure times were 20.8{28.6 ksec in K_s, 13.92{18.12 ksec in H and 7.92{15.12 ksec in J.

For our purposes the only further processing required was to mosaic the 8 fields into a single image for each of the three passbands. However, there was considerable variation between these in signal-to-noise and in zero-point, and to take this into account we performed the mosaicing by the following procedure

(i) scaling the images to a common photometric zero-point (that of the first field), and applying these scalings inversely to the weighting maps. Zero-points were also corrected for the Galactic extinction on the CDFS, but this only 0.008 (J), 0.005 (H) and 0.003 (K_s) mag.

(ii) multiplying the scaled images by their scaled weighting maps, and then mosaicing these together using IRAF 'combine' with 'bsets=wcs' (using the supplied astrometry which is sufficiently accurate), and 'scale=none'. The weighting maps were mosaiced in the same way.

(iii) dividing the first of these mosaics by the second, to obtain the final output mosaic (which will have the field 1 zero point);

(vi) to obtain a weighting map for this final image, multiplying the mosaiced weighting maps by a map of the number of images combined at each pixel (given by $n = 8$ the pixel-list image from the first combination in stage ii).

The three final output mosaics, with weighting maps, were then ready to be used for source detection.

3.2 FORS1 I-band Data

The FORS1 data was supplied to us in a raw form as 24 individual, spatially dithered 450s exposures (\approx 10.8 ksec) for each of the 4 pointings. The first step was to subtract an averaged bias frame from each. Median flat fields were prepared from groups of up to 24 exposures, using IRAF 'combine' with 'combine=median, scale=median', then 'homoflat'. Data images were divided by the appropriate flats, and then sky-subtracted using IRAF 'sky'. The dithering offsets from the first exposure (reference) were measured with IRAF 'xregister'. These offsets rounded to the nearest pixel were used as the shifts for combining the 24 sky-subtracted

exposures, giving stacked (\approx 10.8 ksec) images for each of the four fields.

The data included 8 calibration images of 6 different standard-star fields (from the ESO standards list for FORS1). After flat-fielding and sky subtraction, the standard stars' photon counts were measured with 'SEextractor' (see below), and used to fit a photometric equation,

$$I = 2.5 \log \frac{\text{count}}{\text{exptime}} = +26.358 - 0.077(R - I) - 0.120X$$

where the I mag and R - I colours are from the standard-star catalog and X is airmass. For the Vega system and at the zenith, the zeropoint is determined as 26.238, or 32.871 for 450s, or 32.835 with a correction (0.018 mag) for Galactic extinction.

As the four I-band fields overlapped significantly and the signal-to-noise was much more uniform than for the near-IR data, they were mosaiced together simply by (i) scaling the counts in each from the mean airmass of the 24 exposures to the zenith using the airmass term in the photometric equation, (ii) measuring the offsets between the 4 fields using 'xregister' in the overlap regions, (iii) trimming off the noisy edges of each of the four stacked images where the exposure time is less than about half the full 10.8 ksec, (iv) combining the four fields with unweighted 'combine'.

3.3 Source Detection

Sources were detected on the near-IR and I-band data using 'SEextractor' (Bertin and Arnouts 1996), as in Paper I. The magnitudes presented are (unless otherwise stated) 'total' magnitudes, derived by fitting elliptical apertures to each detection. We also measure aperture magnitudes in circular apertures of fixed 2.5 arcsec diameter. Magnitudes are given in the Vega system and can be converted to the AB system as $(K_s; H; J; I)_{AB} = (K_s; H; J; I)_{Vega} + (1.841; 1.373; 0.904; 0.440)$.

Source detection was performed on the Isaac K_s mosaic, with the chosen criterion that a source must exceed 1.4_{sky} above the background in at least 6 contiguous pixels, and with the additional use of a detection filter (3.0 pixel FWHM Gaussian). The mean sky noise was $sky = 23.11 K_s \text{ mag arcsec}^{-2}$ (1.31 mag deeper than the UFTI data of Paper I) with the variations over the mosaic taken into account using the mosaiced weighting map in the source detection. Detections on the low signal-to-noise edges of the mosaic were excluded, leaving a data area of 50.4 arcmin².

Photometry in H and J was obtained simply by positionally registering (to the nearest pixel) the H and J mosaics to the K_s mosaic and then running SEextractor in 'double-image mode' to detect sources in K_s as before and then measure fluxes on the H and J images within the apertures determined from the K_s data.

Sources were detected on the FORS1 I-band image with the criterion that they exceed 1.3_{sky} ($sky = 26.26 I \text{ mag arcsec}^{-2}$) in at least 6 pixels, and with the use of a 2.5 pixel FWHM Gaussian detection filter.

3.4 K_s-band Galaxy Counts

Star-galaxy separation was performed on the K_s detections using a plot of peak/total flux ratio against magnitude. To K_s = 19.0, 30 objects were classed as stars, and all fainter

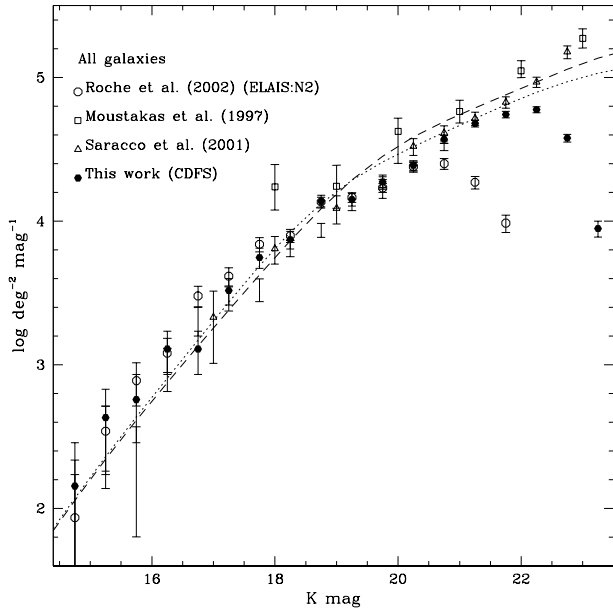


Figure 1. K-band differential number counts of galaxies (of all colours) on the Isaac CDFS and ELAIS-N2 (Paper I) fields (shown well beyond completeness to illustrate the difference in depth), and from the even the deeper surveys of Moustakas et al. (1997) and Saracco et al. (2001) (the small difference between K_s and the 2.2 μ m K-band of the UFTI data is neglected here). Also plotted are PLE (dotted) and $R = R_m = 0.3$ merging (dashed) models (as in Paper I but with $h = 0.7$.)

detections were assumed to be galaxies. The mean Gaussian FWHM of the stars was only 0.46 arcsec, indicating excellent resolution.

Figure 1 shows the differential number count of K_s detections classed as galaxies, shown with the other counts and two models from Paper I. Our CDFS galaxy counts agree well with our (Paper I) ELAIS-N2 counts to $K < 21$, and reach 1.5 mag deeper, turning over only at $K_s > 22$. Comparison with the two even deeper K surveys suggests we are near-complete to $K_s < 21.5$ with moderate (~ 20 per cent) incompleteness at $21.5 < K_s < 22$.

4 SELECTION OF THE ERO SAMPLE

4.1 Identifying the EROs

EROs are essentially galaxies with the red colours expected for high-redshift ellipticals. In Paper I they were selected on the basis of a colour $R - K > 5.0$, while some authors have used a stricter ERO criterion of $I - K > 4.0$ or $R - K > 5.3$ (e.g. Mannucci et al. 2002). In this paper we shall consider both $I - K_s > 3.75$ and $I - K_s > 4.0$ samples, which are approximately equivalent to $R - K > 5.0$ and $R - K > 5.3$ respectively, and to our evolving E/S0 models at $z > 0.99$ and $z > 1.09$.

The first step was to match all K_s detections with their closest I-band detection within a maximum radius of 1.5 arcsec, using the astrometry supplied with the data. This revealed a small positional mismatch of ~ 1 arcsec, and so

to improve the reliability of matching, we fitted (with IRAF `plotool`) an astrometric transform relating the RA and Dec co-ordinates of the stars on the Isaac data to their pixel co-ordinates on the FORS1 mosaic, with rms errors of only 0.19 arcsec. This was used to again match the K_s and I detections, this time within a maximum radius 1.3 arcsec (chosen to optimally avoid mismatching while allowing for extended galaxies), and hence obtain $I - K_s$ colours.

Matching the K_s detections to their H and J counterparts was more straightforward, as the use of double-image mode meant there were no positional offsets.

A list of candidate EROs was selected as all $K_s < 22.0$ galaxies (this limit chosen on the basis of the number count turnover) with either $I - K_s > 3.75$ (108 galaxies), or no detection in I (155 galaxies).

However, not all of the latter will be genuine EROs (some are, for example, bluer galaxies which were individually detected in K_s , but not matched with their R band counterparts because these were confused with neighbouring brighter objects, shifting their detection centroid outside of the matching radius. To filter these 155 candidate EROs, we measured aperture (2.5 arcsec diameter) magnitudes on the I-band mosaic (using IRAF `lphot`) at the positions given by their detections on the Isaac data, combined these with SExtractor K_s -band aperture magnitudes to estimate $I - K_s$ aperture colours, and then only accepted the objects with $(I - K_s)_{\text{aperture}} > 3.75$, which numbered 92. This method appeared to reliably exclude the confused objects.

Our ERO ($I - K_s > 3.75$) sample then consisted of a total of 200 galaxies with $K < 22.0$, of which 163 satisfied the stricter criterion of $I - K_s > 4.0$. These samples make up the reddest 12.4 and 10.1 per cent of all $K < 22$ galaxies detected (1619).

4.2 Colours of EROs

ERO colours correspond to passive galaxies at approximately $z > 1$, where the observer-frame K-band and the R or I-band will bracket the large break at 4000Å rest-frame. However, any type of galaxy, including a young starburst, could be this red if sufficiently dusty. Figure 2a shows models of $I - K_s$ against redshift, representing an elliptical galaxy (solid line) which forms all its stars in a 1 Gyr burst at $6.0 > z > 3.4$, and an S0 galaxy with a 2 Gyr burst continuing to $z = 2.6$, with $E(B - V) = 0.4$ mag dust reddening during the bursts and subsequent unreddened passive evolution, both giving ERO colours at $z > 1$.

Dusty starburst models are also plotted (dot-dash and dotted lines), represented as non-evolving starbursts observed at age 50 Myr with two high values of the dust-reddening. Evidently these can produce the same $I - K_s$ colours as passive galaxies, especially at $z > 1$, although if very dusty they can enter the $I - K_s > 3.75$ range at $z < 0.5$ (1.0). Older star-forming galaxies, or recent post-starbursts, would have intermediate spectra and could be EROs with moderate reddening.

Figure 2b shows $I - K_s$ for all $K < 22$ Isaac detections, with aperture colours for the EROs undetected in I. As in Paper I, EROs appear at $K_s < 18$.

With the H-K and J-K colours provided by the Isaac data, it is also possible to achieve an approximate

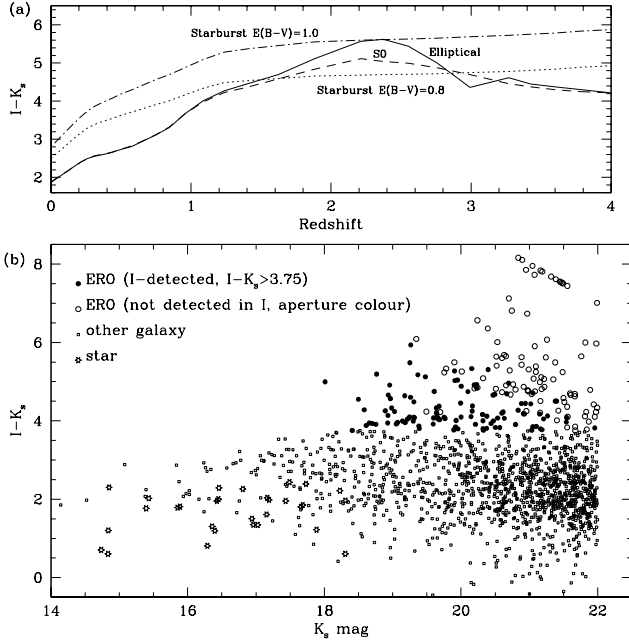


Figure 2. (a) Observer-frame $I-K_s$ colour (Vega system) against redshift for models representing evolving elliptical (solid) and S0 (dashed lines) galaxies and dust-reddened young starbursts (dotted/dot-dash lines), (b) Observed $I-K_s$ colours of all $K_s < 22$ detections on the Isaac data, with larger symbols indicating the 200 $I-K_s > 3.75$ EROs. The colours are based on 'SExtractor' total magnitudes, except for EROs undetected in I, for which colours are measured in 2.5 arcsec diameter apertures.

separation of passive and dusty, star-forming EROs (pEROs and dsfEROs). Pozzetti and Mannucci (2000) describe how these types can be separated on a plot of $I-K$ against $J-K$, although this is only possible at $1 < z < 2$, where the redshifted 4000Å break lies between the I and J bands. Here, we use essentially the same method, but also incorporate the $H-K$ colour, which extends this method to $z > 2.5$.

Figure 3 shows $I-K_s$ against $J+H-2K_s$ (i.e. the sum of $J-K_s$ and $H-K_s$) with the diagonal line showing the adopted pERO/dsfERO divide, at $J+H-2K_s = 0.67(I-K_s) + 0.08$.

Most of these EROs have colours consistent with either the passive models at $1 < z < 2.5$ or the $E(B-V) \sim 0.8$ starburst at $z < 2$. However, many lie close to the dividing line, whether this is due to scatter in the magnitudes or to genuinely intermediate spectra. Of the $K_s < 22$ galaxies with $I-K_s > 3.75$ (410), we classify 116 (104) as pEROs and 84 (59) as dsfEROs.

4.3 Distribution on the Sky

Figure 4 shows the distribution of the ERO sample, and the 73 Chandra detections (Giacconi et al. 2002) on the Isaac mosaic area of the CDFS. The EROs appear somewhat clustered on small scales, and a particularly obvious clump, consisting of mostly pEROs and centred on Chandra source XID 58 (R.A. $3^h 32^m 11.85^s$ Dec $-27^{\circ} 46' 29.14''$), is highlighted on the plot, and discussed further in Section 7.1.

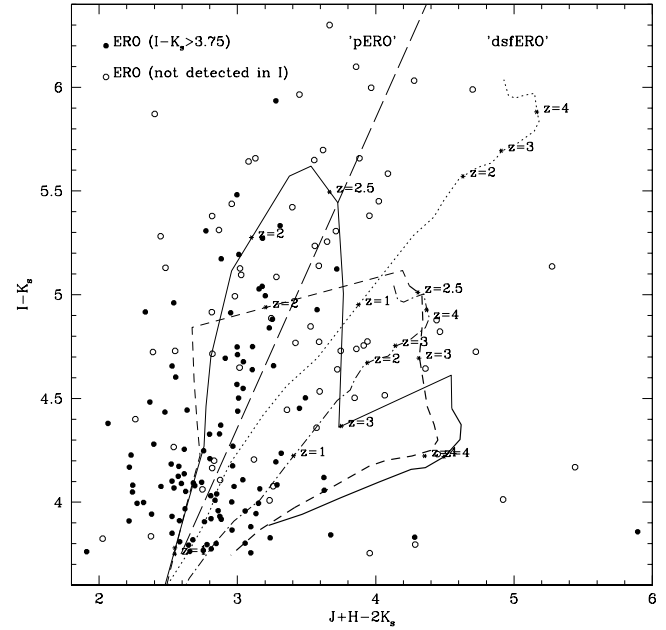


Figure 3. Plot of $I-K_s$ vs. $J+H-2K_s$ for all $K_s < 22$ EROs (with aperture colours for those undetected in I, otherwise total mag colours). Also plotted are the elliptical (solid) and S0 (short-dashed) models, with redshifts marked, and heavier lines indicating the redshift range of the formative starbursts, and starburst models with reddening $E(B-V) = 0.8$ (dotted) and 1.0 magnitudes (dot-dash). The long-dashed diagonal line shows an approximate separation of the pERO and dsfERO types.

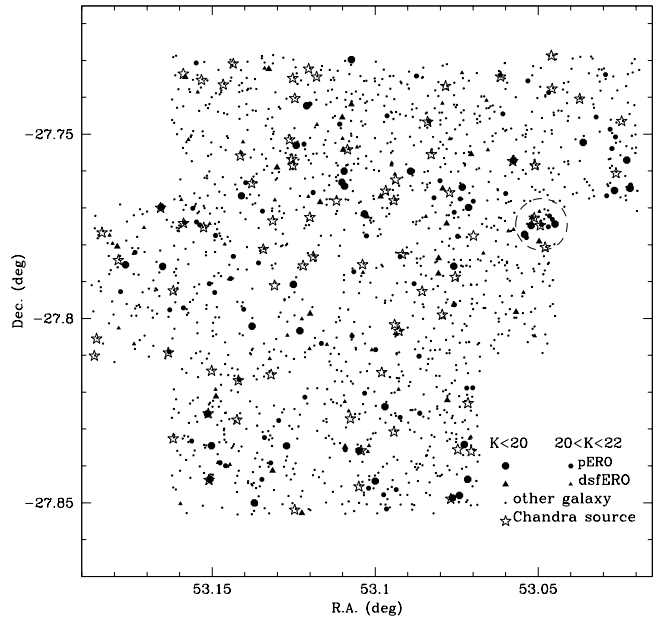


Figure 4. Distribution of colour-classified pEROs and dsfEROs, other detected galaxies and Chandra X-ray sources, on the area of the CDFS covered by the Isaac data. The dashed circle indicates a possible cluster of EROs centered on the Chandra source XID 58.

Table 1. Observed number counts (number of galaxies N_g and surface density (in units $\text{deg}^{-2} \text{mag}^{-1}$, with $^{\pm} N$ errors) of galaxies with $I - K_s > 3.75$ and $I - K_s > 4.0$ (EROs) on the CDFS.

K_s	$I - K_s > 3.75$		$I - K_s > 4.0$	
	N_g	N_g	N_g	N_g
< 18:0	0	0	0	0
18.0{18.5}	3	429	276	2
18.5{19.0}	13	1858	515	8
19.0{19.5}	22	3145	670	15
19.5{20.0}	24	3431	700	20
20.0{20.5}	28	4003	756	22
20.5{21.0}	40	5718	904	37
21.0{21.5}	42	6004	926	37
21.5{22.0}	28	4003	756	22

(significantly incomplete)

5 NUMBER COUNTS OF EROS

5.1 Observed counts on the CDFS

Table 1 gives our CDFS ERO counts for both selection limits. Figure 5 shows differential number counts for $I - K_s > 3.75$ or $R - K > 5.0$ EROs. The most obvious feature is a marked attening of the count slope, from $\alpha = 0.66 \pm 0.11$ at $17.0 < K_s < 19.5$ (best-fit to the ELAIS-N2 and CDFS counts) to $\alpha = 0.16 \pm 0.05$ at $19.0 < K_s < 21.5$ (CDFS counts). In Paper I we applied an estimated incompleteness-correction to our counts at $20 < K_s < 21$ (as shown here), but for the CDFS we simply assume completeness to $K_s = 21.5$ and disregard the tail point, which shows a sudden drop in ERO numbers (incompleteness will appear more suddenly for this data due to its more uniform depth).

Figure 6 shows counts of $I - K_s > 4.0$ or $R - K > 5.3$ EROs, including $R - K > 5.3$ galaxy counts for the ELAIS-N2 field, as derived from the UFTI/Ingrid source catalog of Paper I.

5.2 ERO counts: Models and interpretation

In Paper I we presented simple models of the number counts of EROs, based on the assumption that they are all progenitors of the present day E/S0 galaxies and hence their luminosity function (LF) at any redshift can be linked to the LF of local E/S0s by means of a particular evolutionary model. We adopted the local E/S0 LF derived by Kochanek et al. (2001) in the K-band, from the MASS survey, a Schechter function with $M_K = -24.31$, $\alpha = 0.92$ and $\phi = 0.0015435 \text{ Mpc}^{-3}$ for $h = 0.7$. The ERO counts were modelled by evolving this LF with the galaxies split 50:50 between our elliptical and S0 models of L evolution, and including only the galaxies within the redshift ranges in which their respective models give colours redder than the ERO colour selection (i.e. approx. $z > 1$).

In the Pure Luminosity Evolution (PLE) model only L is evolved, while α and ϕ remain constant from the formation redshift onwards. In Paper I, the ERO number counts on ELAIS-N2 were significantly lower than expected if all present-day E/S0s evolved by this PLE model, and much closer to a non-evolving model. However, this was inconsistent with the compact angular sizes of most EROs, which implied significant evolution in surface brightness. We also

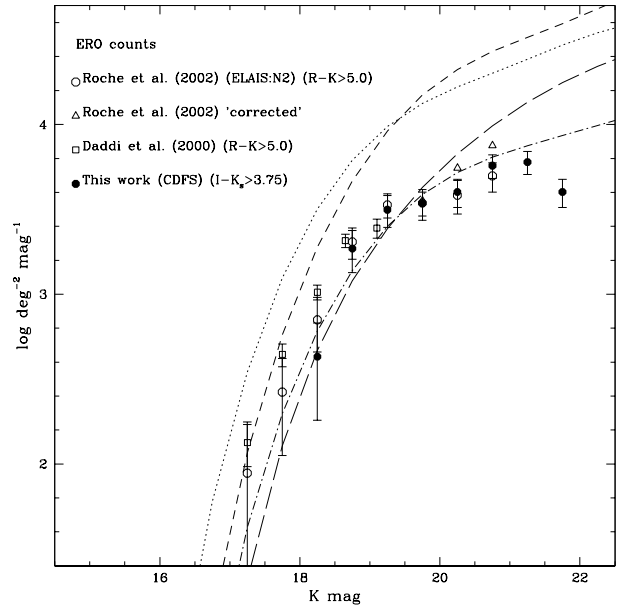


Figure 5. K-band differential number counts for $I - K_s > 3.75$ EROs on the CDFS together with EROs selected at a comparable limit of $R - K > 5.0$ on the ELAIS-N2 field (Paper I/Roche et al. 2002), and from Daddi et al. (2000), compared with the counts of $I - K_s > 3.75$ galaxies predicted by PLE (dotted), non-evolving (long-dashed), merging with $R = R_m = 0.3$ (short-dashed), and M-DE merging with $R_m = 0.3$, $R = 0.5$ (dot-dashed) models. Error bars are $^{\pm} N$.

tried a merging model which combined the modelled evolution of luminosity (per unit mass) with an increase with redshift in galaxy number density (ϕ) and a corresponding decrease in mass (parameterized as $R = R_m = 0.3$; see Paper I), based on an observational estimate of the merger rate and its evolution (Patton et al. 2002). This also over-predicted the ERO counts.

However, by keeping the mass evolution at $R_m = 0.3$ and varying the density evolution to fit the counts, a reasonable best-fit was obtained for $R = 0.46$ (0.10). In this 'merging and negative density evolution' (M-DE) model, the comoving number density of passive galaxies (or any galaxies of similar colour) gradually decreases with redshift. Physically, this could result from some fraction of the present-day massive ellipticals forming at high (e.g. $z > 3$) redshifts, with the remainder forming from bluer galaxies (e.g. through interactions and mergers) at all intermediate redshifts.

Figures 5 and 6 compare the ERO counts with, respectively, PLE, merging ($R = R_m = 0.3$) and non-evolving models. The fourth model plotted is M-DE, with a new value of the ERO density evolution, $R = 0.50$ (0.06), estimated by best-fitting to the $I - K_s > 3.75$ CDFS counts at $K = 21.5$. In this model the evolution of the characteristic mass (from merging) is (as in Paper I), $\phi(z = 1; 2; 3) = (0.714; 0.558; 0.493) \text{ Mpc}^{-3}$ ($z = 0$), and the comoving number density of passive/red galaxies evolves as $\phi(z = 1; 2; 3) = (0.570; 0.378; 0.308) \text{ Mpc}^{-3}$ ($z = 0$).

Again the PLE and merging models overpredict all the observation. Our deep CDFS counts are consistent with the

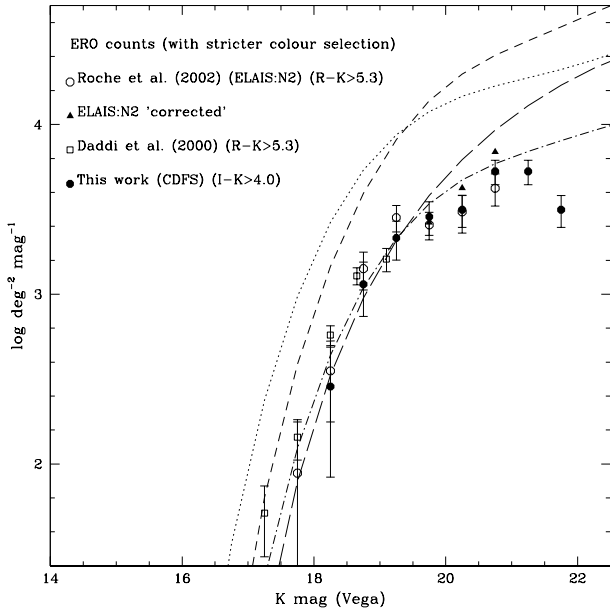


Figure 6. K-band differential number counts for $I - K_s > 4.0$ EROs on the CDFS together with EROs selected at a comparable limit of $R - K > 5.3$ on the ELAIS-N2 field (from catalog of Roche et al. 2002), and from Daddi et al. (2000), compared with counts of $I - K_s > 4.0$ galaxies predicted by the same models as shown on Figure 5. Error bars are 1σ .

non-evolving model at brighter magnitudes, but fall below it at $K > 20$ after attenuating significantly. This is an important result as it implies that the discrepancy with PLE reflects a decrease in the comoving number density of these galaxies and not only the effects of merging on mass/luminosity.

The counts on Figures 5 and 6 are clearly most consistent with M-DE. On Figure 5 there is some excess over the model at $K < 19$, but this disappears on Figure 6, indicating that it consists of borderline-ERO colour galaxies (these might be a 'contamination' of the sample by dust-reddened galaxies at redshifts lower than 1). We conclude that the deeper ERO counts from the CDFS provide further evidence for the M-DE' type of evolution.

6 CLUSTERING OF THE EROS

6.1 Calculating $\xi(r)$

To investigate the clustering of EROs on the CDFS, and compare it with other galaxies, we calculate the angular correlation function, $\xi(r)$, for (a) all galaxies (of any colour) to a series of K_s magnitude limits, (b) all EROs for both $I - K_s > 3.75$ and $I - K_s > 4.0$ selections, (c) pEROs and dsfEROs considered separately. The method adopted is exactly as described in Paper I, with the use of $N_r = 50000$ random points.

In addition, (d) we calculate the angular cross-correlation of the pEROs and dsfEROs, as

$$\xi_{pd}(r) = \frac{N_{pd}(r) N_d}{N_{pr}(r) N_r} - 1$$

where $N_{pd}(r)$ is the total number of pERO {dsfERO pairs (centering on the pEROs) in the r interval of angular separation, $N_{pd}(r)$ the number of pERO {random point pairs, N_d the number of dsfEROs and N_r the number of random points. As an additional check, we also evaluated the cross-correlations with centering on the dsfEROs, i.e. as

$$\xi_{dp}(r) = \frac{N_{dp}(r) N_p}{N_{dr}(r) N_r} - 1$$

which gave essentially the same results ($\xi_{dp} \approx \xi_{pd}$ at all r , to within a small fraction of the statistical errors, 0.1).

At the small r considered here, the galaxy $\xi(r)$ is an approximate power-law $\xi(r) \approx A_1 r^{-0.8}$, which follows from their 3-dimensional two-point correlation function in physical separation (r), $\xi(r) = (\frac{r}{r_0})^{-1.8}$. We therefore, as previously, express the $\xi(r)$ results in the form of an amplitude A_1 at $r = 1$ deg. We obtain this by fitting the observed $\xi(r)$ with the function $A_1 (r^{-0.8} / 12.24)^{-1.8}$ (where 12.24 is the 'integral constraint' as determined for the Isaac field area; see Paper I), over the range of separations $2 < r < 32$ arcsec. Error bars were estimated by the method described in Paper I, using 12 'sub-areas', and are generally a little larger than 1σ errors.

6.2 $\xi(r)$ Results

Table 2 gives our A_1 amplitudes for a range of magnitude limits (these results may be less reliable at $K_s > 21.5$ due to incompleteness), and Figure 7 shows example $\xi(r)$ with fitted power-laws.

Positive clustering is detected, at $3\{4$ for all galaxies and $2\{3\{6$ for the EROs. The $\xi(r)$ amplitude of EROs is always much ($4\{10$ times) higher than that of all galaxies at the same K_s limit, and slightly higher for the $I - K_s > 4$ than for the $I - K_s > 3.75$ selection, although the difference is not large.

Table 3 also gives the A_1 for the pERO and dsfERO subsamples. Unfortunately it seems that our sample is insufficient to determine whether these differ in their clustering properties. We do find at 2 that the pEROs considered separately are clustered, with a similar amplitude to the full ERO sample. The dsfERO A_1 has a similar best-fit amplitude, but, as the signal is only 1 , would still be consistent with the very weak dsfERO clustering reported by Daddi et al. (2002). The cross-correlation may be marginally weaker than the pERO autocorrelation, which may hint at some segregation of the types (and/or a difference in their $N(z)$), but more data are needed.

6.3 Interpretation of the $\xi(r)$

The observed $\xi(r)$ of any sample of galaxies will depend on their intrinsic clustering in 3D space, described by the two-point correlation function $\xi(r)$, and their redshift distribution $N(z)$. If $\xi(r)$ is represented by the simple model

$$\xi(r; z) = (\frac{r}{r_0})^{-1.8} (1+z)^{(3+\beta)}$$

where r_0 is the local correlation radius, $\beta = 1.8$ (observationally) and β represents the clustering evolution ($\beta = 0$ is stable and $\beta = 1.2$ is comoving clustering), then Linber's

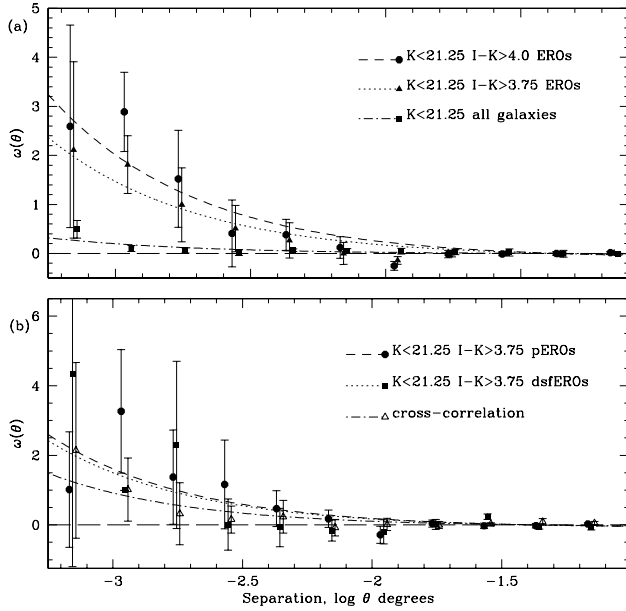


Figure 7. (a) Angular correlation functions $\xi(\theta)$ for $I - K > 4.0$ EROs, $I - K > 3.75$ EROs and galaxies of all colours on the Isaac CDFS data, to $K = 21.25$ (slightly offset horizontally for clarity), with the dashed, dotted and dot-dash lines showing their respective best-fitting functions of the form $A_1 (1 + z)^{-1.24}$; (b) $\xi(\theta)$ of $I - K > 3.75$ $K < 21.25$ EROs of pERO and dsfERO colour-classification, and their cross-correlation function, again with the dashed, dotted and dot-dash lines showing their respective best-fitting $A_1 (1 + z)^{-1.24}$.

formula gives $\xi(\theta) = A_1 (1 + z)^{-1}$, where

$$A_1 = C r_0 \int_0^{z_1} \frac{(1+z)^{-(3+\epsilon)}}{x^2(z) \frac{dx(z)}{dz}} [N(z)^2] dz = \left[\int_0^{z_1} N(z) dz \right]^2$$

where $x(z)$ is the proper distance and $C = 3.679$ for $\epsilon = 1.8$.

We model the $N(z)$ of EROs (Figure 8) using the M-DE' model with $R = 0.50$.

Before considering the EROs we briefly investigate the $\xi(\theta)$ scaling of the full K -limited galaxy sample. We model this using $N(z)$ from the $R_{\text{phi}} = R_m = 0.3$ merging model of Paper I, and local correlation radius of $r_0 = 5.85 h^{-1} \text{ Mpc}$, estimated from an $I < 22$ survey (Cabanac, de Lapparent and Hickson 2000), for both stable and comoving clustering. The observations (Figure 9) lie mostly between the two but closer to the stable model, suggesting $\epsilon = 0.4$ (also plotted).

Figure 10 shows the A_1 scaling of $I - K_s > 3.75$ or $R - K < 5.0$ EROs. We model the $\xi(\theta)$ with the M-DE $N(z)$ and vary the r_0 normalization to best-fit (minimize χ^2) for all the plotted data points, and in this way estimate the intrinsic clustering of EROs as $r_0 = 11.7 (1.3) h^{-1} \text{ Mpc}$ ($\frac{r_0}{h^{-1}} = 1.52$) for comoving and $r_0 = 20.3 (2.3) h^{-1} \text{ Mpc}$ ($\frac{r_0}{h^{-1}} = 1.07$) for stable clustering.

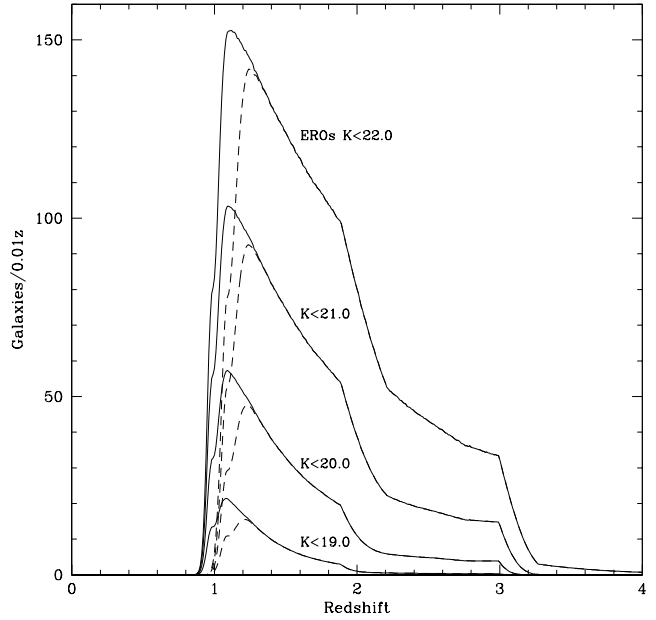


Figure 8. $N(z)$ for $I - K_s > 3.75$ EROs as given by $R = 0.54$ M-DE' model, at limits $K_s = 19.0, 20.0, 21.0, 22.0$ (solid lines). The dashed lines show the higher low-redshift cut-off for $I - K_s > 4.0$ EROs.

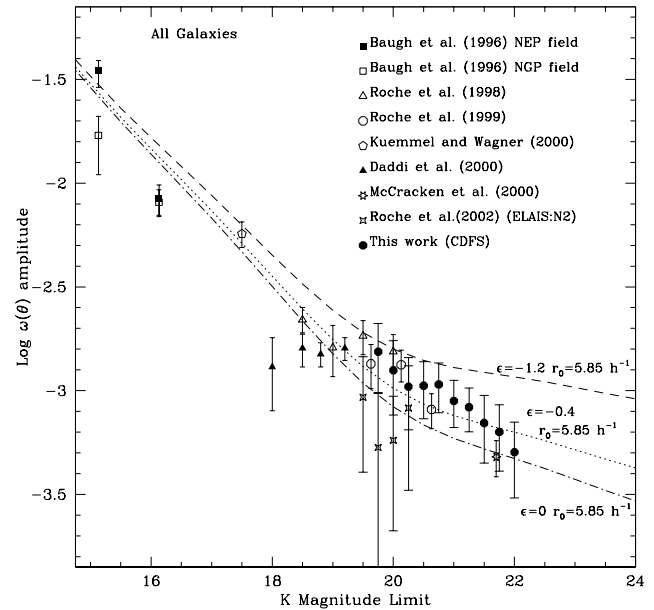


Figure 9. The scaling of $\xi(\theta)$ amplitude with K magnitude limit for full K -limited samples of galaxies, as derived from our Isaac CDFS data and from previously published results, with models (all with $r_0 = 5.85 h^{-1} \text{ Mpc}$) of stable ($\epsilon = 0$) and comoving ($\epsilon = 1.2$) clustering and an intermediate ($\epsilon = 0.4$) evolution.

Table 2. Galaxy $\delta(\theta)$ amplitudes A_{δ} (in units of 10^{-4} at one degree) of full K_s -limited samples and I $K_s > 3:75$ and I $K_s > 4:0$ EROs, to a series of magnitude limits. N_g is the number of galaxies in each sample. The A_{δ} of EROs is not given for the first three limits as the samples are too small for any detection of clustering.

K_s mag limit	All galaxies			I $K_s > 3:75$			I $K_s > 4:0$		
	N_g	A_{δ}		N_g	A_{δ}		N_g	A_{δ}	
19.75	391	15:40	5:74	49			35		
20.00	467	12:53	4:89	62			45		
20.25	558	10:45	3:98	77			59		
20.50	638	10:56	3:23	90	52:6	28:5	67	56:0	32:4
20.75	770	10:71	2:88	111	39:3	15:0	86	46:2	23:6
21.00	898	8:92	2:28	130	62:3	20:8	104	79:6	21:8
21.25	1067	8:32	1:99	157	61:4	19:5	126	84:1	23:7
21.50	1233	6:98	2:50	173	44:3	16:1	142	59:8	18:2
21.75	1432	6:32	2:24	186	38:4	14:6	151	54:2	16:1
22.00	1619	5:05	2:01	200	32:4	13:5	163	40:8	14:1

Table 3. Galaxy $\delta(\theta)$ amplitudes A_{δ} (in units of 10^{-4} at one degree) for the colour-selected pERO and dsfERO subsamples of the I $K_s > 3:75$ EROs, the numbers N_g of each, and their cross-correlation amplitude, to a range of K_s magnitude limits.

K_s mag limit	pEROs			dsfEROs			pERO dsfERO	
	N_g	A_{δ}		N_g	A_{δ}		A_{δ}	
20.5	57	47:5	35:0	33	35:4	59:4	27:1	42:0
20.75	68	71:0	40:0	43	115:1	126:6	13:1	18:6
21.0	79	100:7	37:9	51	73:5	88:8	25:4	23:0
21.25	96	67:5	33:8	61	62:9	74:3	38:6	35:2
21.5	108	44:3	24:1	65	65:5	65:3	25:1	30:3
21.75	112	38:4	21:4	74	73:9	55:1	20:8	27:0
22.0	116	57:7	30:8	84	49:0	38:6	13:3	22:7

Table 4. EROs detected as X-ray sources: Chandra source XID number (Gialalisco et al. 2002), detection number on the K_s mosaic, RA and Dec of K_s -band detection, K_s magnitude (total), I K_s colour, ERO colour classification, Soft and Hard X-ray fluxes in units of 10^{-16} erg s $^{-1}$ cm $^{-2}$, and X-ray hardness ratio HR (see text).

XID	det.	RA	Dec.	K_s	I K_s	p/dsf	F (0.5{2:0 keV)	F (2{10 keV)	HR					
26	1527	3:32:39.75	-27:46:11.25	19:64	0:09	4:21	0:11	p	7:35	0:750	28:9	4:07	0:23	0:08
58	1435	3:32:11.76	-27:46:28.14	20:94	0:17	4:44	0:26	p	6:36	0:668	18:8	3:26	0:36	0:09
79	1446	3:32:38.04	-27:46:26.26	20:92	0:11	4:89	0:35	p	8:06	0:785	20:7	3:64	0:42	0:08
81	2425	3:32:25.93	-27:45:14.27	21:40	0:17	4:50	0:23	dsf	3:74	0:517	9:11	2:59	0:44	0:13
86	1868	3:32:33.84	-27:45:18.08	20:38	0:10	4:12	0:15	dsf	1:22	0:345	6:96	2:43	0:05	0:22
145	1589	3:32:22.54	-27:46:03.80	20:32	0:10	4:00	0:12	dsf	3:17	0:463	34:5	3:89	0:27	0:09
153	69	3:32:18.32	-27:50:55.25	18:58	0:04	4:28	0:06	p	1:88	0:403	46:6	4:43	0:59	0:07
221	2037	3:32:08.91	-27:44:24.81	21:76	0:16	5:66 ^[1]	1:78	dsf	1:09	0:360	< 5:12		1:00 ⁺	0:84
253	2112	3:32:20.05	-27:44:47.20	20:00	0:09	4:10	0:13	p	0:829	0:320	26:0	3:52	0:66	0:11
513	608	3:32:34.01	-27:48:59.74	21:19	0:17	> 5:5 ^[1]		p	0:847	0:331	8:60	2:60	0:23	0:23
515	1303	3:32:32.17	-27:46:51.49	21:99	0:19	4:36 ^[1]	0:59	dsf	0:843	0:304	12:7	2:74	0:41	0:17
593	2554	3:32:14.79	-27:44:02.49	21:21	0:12	4:05	0:23	p	0:857	0:313	< 4:60		1:00 ⁺	0:90
600	2252	3:32:13.81	-27:45:25.63	18:66	0:03	3:94	0:05	p	< 0:548		18:8	3:26	1:00	0:66
605	731	3:32:39.18	-27:48:32.35	21:26	0:15	6:10 ^[1]	1:38	p	< 0:654		5:68	2:44	1:00	0:86
609	148	3:32:36.17	-27:50:36.93	19:64	0:07	4:33	0:11	p	< 0:687		9:31	2:63	1:00	0:65
623	1245	3:32:28.51	-27:46:58.17	20:60	0:09	4:64 ^[1]	0:23	dsf	0:809	0:300	< 4:49		1:00 ⁺	0:92

[1] Object below detection threshold in I-band. Colour measured in 2.5 arcsec diameter aperture.

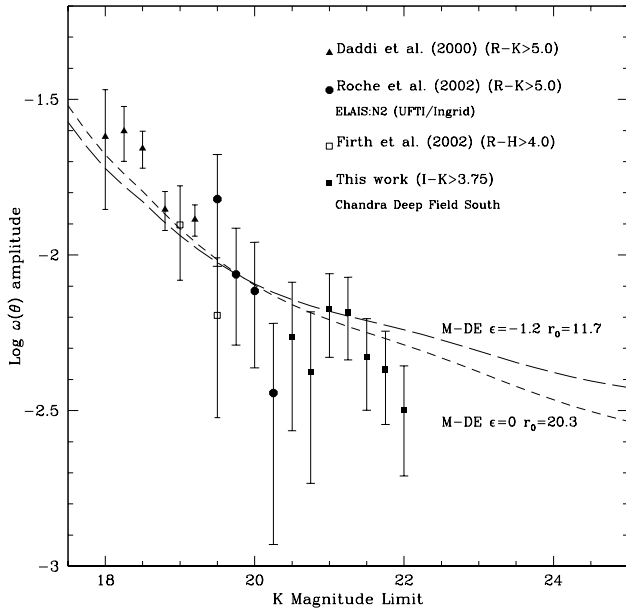


Figure 10. The scaling of $\omega(\theta)$ amplitude with K magnitude limit for EROs selected as $I-K_s > 3.75$ or $R-K > 5.0$, from our IsaacCDFs data and from previously published results, compared with M-DE models with either stable ($\epsilon = 0$) or comoving ($\epsilon = -1.2$) clustering and r_0 best-fitted to the plotted data points.

Figure 11 shows the A_1 scaling of EROs selected by the stricter criteria of $I-K_s > 4.0$ or $R-K > 5.3$. Estimating their r_0 by the same method gives $r_0 = 11.2$ (± 1.7) h^{-1} Mpc ($\frac{\sigma}{N} = 0.61$) for comoving and $r_0 = 20.4$ (± 2.5) h^{-1} Mpc ($\frac{\sigma}{N} = 0.52$) for stable clustering. The A_1 are slightly higher for $I-K_s > 4.0$ than for $I-K_s > 3.75$ EROs, but this appears to be accounted for in Limber's formula by their narrower $N(z)$, as their best-fit r_0 are near-identical.

7 ERO CLUSTERS AND PAIRS

7.1 A possible cluster of EROs

In Paper I we noted a possible cluster of EROs in the ELAIS-N2 field, centered on a bright ERO which is also a Chandra source and radio galaxy. In the CDFS, we find another overdensity of EROs, centered on Chandra source XID 58 (R.A. $3^h 32^m 11.85^s$ Dec $-27^{\circ} 46' 29.14''$), a somewhat fainter ERO ($K_s = 20.94$, $I = 25.39$, $J = 21.56$, $H = 22.96$). Within a 20 arcsec radius there are a total of 11 $K < 22.0$, $I-K_s > 3.75$ (10 with $I-K_s > 4.0$) galaxies compared to 1.39 (1.13 with $I-K_s > 4.0$) expected from their mean surface density. There is no accompanying overdensity of bluer ($I-K_s < 3.75$) galaxies (8 are seen compared to 9.83 expected).

Figure 12 shows this region on the Isaac image with EROs and Chandra sources marked, and Figure 13 shows these 11 EROs on a colour-colour plot. Firstly, the overdensity is composed primarily of passive EROs, as might be expected for a cluster-centre environment. Six of the 8 pEROs in this area, including the Chandra source, are also

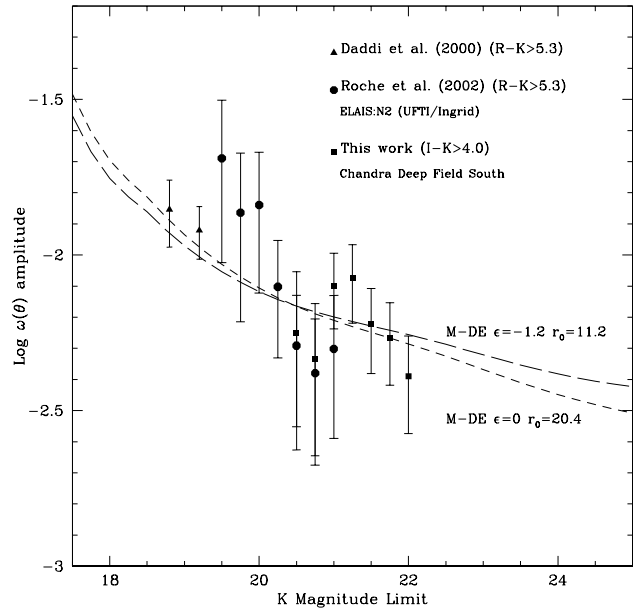


Figure 11. As Figure 10 for EROs selected as $I-K_s > 4.0$ or $R-K > 5.3$ galaxies.

clustered on the colour plot, in the region of the E/S0 models at $z = 1.5\{1.6$, and a seventh pERO (with $K_s = 21.16$) is at least consistent with this redshift.

A recent photometric redshift estimate for the XID 58 galaxy (Mainieri 2003) gives $z = 1.44$. Assuming this redshift, (i) the $r = 20$ arcsec scale of the overdensity is 0.233 Mpc for $h = 0.7$, (ii) the absolute magnitude of XID 58 (from our pERO model and the observed K_s mag) is $M_R = -22.05$ for $h = 0.7$, which, allowing for this model's 1.26 mag of R-band evolution since this redshift, and comparing with the local $M_R = -21.5$ (Kukula et al. 2003) implies a mass only $0.5 L_{\odot}$. The X-ray flux of $F(0.5\{2.0$ keV) = 6.36 (± 0.668) $\times 10^{-16}$ and $F(2.0\{10.0$ keV) = 1.88 (± 0.326) $\times 10^{-15}$ ergs $\text{cm}^{-2} \text{s}^{-1}$ would, for a $f_{\text{X}} = 1$ SED, corresponds to $L_X(0.5\{10.0$ keV) $\sim 10^{43.5}$ ergs s^{-1} for $h = 0.7$. This is too high for a starburst or normal elliptical (see Section 8), and the X-ray flux cannot be produced by hot intracluster gas as it is point-like with no detectable diffuse component (Giacconi et al. 2002), and hence must be from an obscured AGN within the pERO.

The colours of the 8th pERO ($K_s = 20.39$) suggest it is at $z = 2$ and not associated with the others. Redshift estimation is more difficult for dsEROs, but, if we consider a 'reddening locus' as a straight line intersecting the two plotted dsERO models at $z = 1.5\{1.6$, the colours of the $K_s = 19.03$ and $K_s = 21.67$ dsEROs appear at least consistent with this redshift, although spectroscopy would be needed to confirm this.

The $K_s = 19.92$ dsERO, the only one with $I-K_s < 4.0$, appears to be interacting with a brighter ($K_s = 18.35$) non-ERO close neighbour, which coincides with a second Chandra source, XID 149. This X-ray source galaxy now has a spectroscopic redshift of 1.033 (Szokoly et al. 2003), so neither galaxy can be associated with the cluster.

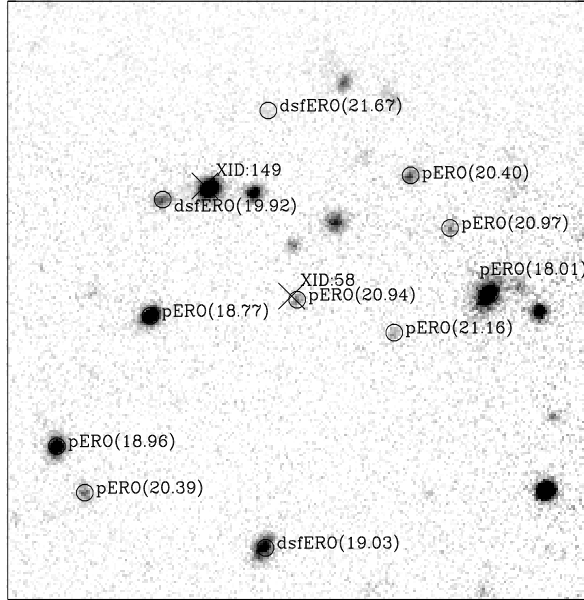


Figure 12. Greyscale plot of the 40×40 arcmin region of the Isaac Newton Telescope (INT) field centred on the Chandra source XID 58. X-ray source positions are labelled with XID numbers from Giacconi et al. (2002) and EROs by their pERO or dsfERO classification and K_s magnitude (in brackets).

A notable difference from the possible $z \sim 1.1$ cluster of Paper I is that the central X-ray source is not the brightest ERO; in fact it is ranked 5th in K_s magnitude out of the 7 possible cluster pEROs at $r < 20$ arcsec. This lack of central mass concentration, together with the non-detection of diffuse X-ray emission, may indicate a forming cluster in an early stage of dynamic evolution.

In summary, there appears to be evidence for the existence of a cluster or proto-cluster at $z \sim 1.5$, consisting primarily or entirely of passive EROs, with 7 to 9 $K_s > 22$ EROs within a 20 arcsec radius, and centered on the obscured-AGN elliptical XID 58. It should be possible to confirm (or exclude) this as several of the EROs may be within the reach of spectroscopy.

7.2 Close pairs of Galaxies, and the Merger rate

The number of pairs of galaxies at very close separations, $< 40 h^{-1} \text{ kpc} \approx 5$ arcsec at ERO distances, is related primarily to the frequency of interactions and mergers. Patton et al. (1992) estimated that for an optically selected sample of galaxies at $z \sim 0.3$, there were 0.0321 ± 0.007 interacting companions per galaxy, and that this fraction and the merger rate were evolving (at $z < 1$) as $\propto (1+z)^{2.3}$. This

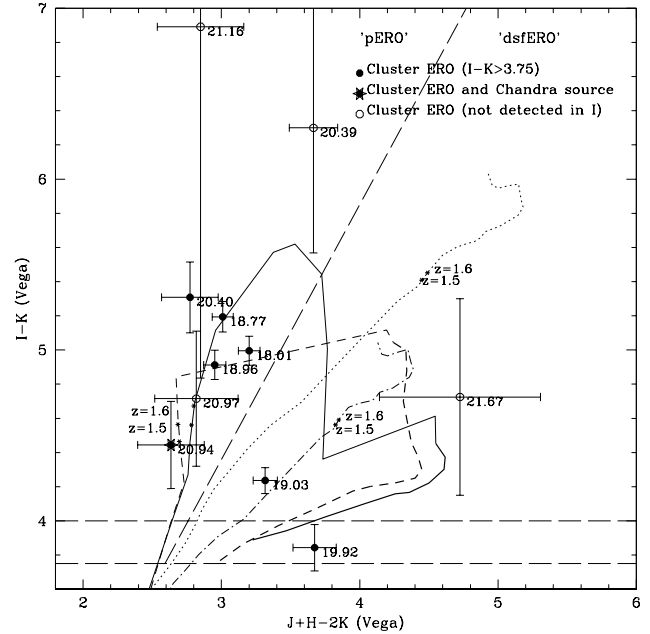


Figure 13. Colour-colour plot of the 11 EROs within a 20 arcsec radius of XID 58. Each ERO is labelled by its K_s magnitude (as on Figure 12). The long-dashed diagonal line shows the pERO/dsfERO divide, the horizontal long-dashed lines the two ERO selection limits. The solid lines show the redshift loci of out E and S0 models with the bolder sections on the right indicating the high- z starburst phase. The dotted line shows the $E(B-V) = 1.0$ dusty starburst model and the dot-dash line this model with $E(B-V) = 0.8$. On each model locus are marked the positions corresponding to redshifts 1.5 and 1.6.

result is incorporated in our merging and M-DE model as $R_m(z) = 0.3(1+z)^{2.3}$ mergers per Hubble time. It also provides a useful point of comparison for the EROs.

To investigate the close-pair counts within our ERO sample, we use a method originally described by Woods, Fahman and Richer (1995). For each pair a probability P of occurring by chance (in a random distribution) is estimated as

$$P = 1 - \exp(-\langle n_2 \rangle \Omega) \quad (1)$$

where $\langle n_2 \rangle$ is the surface density of galaxies in the sample brighter than m_2 , the apparent magnitude of the fainter galaxy of the pair, Ω is the area of the annulus around the brighter galaxy between θ_1 and θ_2 , an angular separation cut-off below which individual objects cannot be resolved ($\theta_1 \approx 1$ arcsec here), and θ_2 , the pair separation, which is included in the observed area (hence $\Omega = \pi(\theta_2^2 - \theta_1^2)$ away from any edges or 'holes'). We estimate $\langle n_2 \rangle$ numerically by counting points distributed randomly and densely over the observed field area.

As in Woods et al. (1995), galaxy pairs with $P < 0.05$ are then counted as close pairs with a high probability that they are interacting. Applying this method to our full $I - K_s > 3.75$, $K_s > 22$ sample of 200 EROs, we found 19 close pairs, of which 10 are pERO (pERO, 4 are dsfERO/dsfERO and 5 are mixed-type. Hence there is no indication that dsfEROs are more likely to be found in interacting pairs

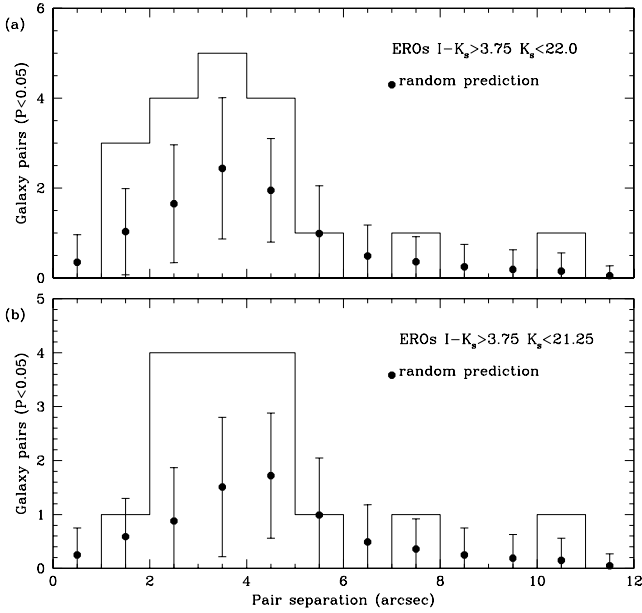


Figure 14. Histogram of the number of close ERO-ERO pairs with $P = 0.05$ (as defined in the text) as a function of pair separation, as calculated for $I - K_s > 3.75$ ERO samples limited at (a) $K_s = 22.0$ (b) $K_s = 21.75$. The plotted points show the expectation for galaxies of the same number and K_s magnitude distributed randomly (from the mean of 100 randomized simulations) with the error bars showing the estimated error interval for a single sample.

than pEROs. However, we must subtract the number of pairs due to chance coincidence. To estimate this, the same analysis is performed on 100 simulations with the same number of galaxies and the same magnitude distribution as the real sample, but randomized positions, and the simulated pair counts are averaged for each bin of pair separation. A small additive correction may also be needed for the number of very close pairs missed due to merging of their images on the CCD frame.

Figure 14a shows the observed ERO pair counts at $K_s < 22$ and random prediction and against separation. The observed counts show an excess at 1.5 arcsec. The only indication that pairs may be missed due to image merging is at < 1 arcsec where 0.35 are expected and none are observed. We estimate a correction for this by assuming the ratio of real to simulation pairs is the same here as at 1.3 arcsec, $\frac{7}{2.68}$, and hence a corrected pair count is $19 + \frac{7}{2.68} \times 0.35 = 19.91$. The random prediction for all separations is 9.90 ± 3.09 (error for a single sample). Subtracting this from the corrected pair count gives 10.01 ± 3.09 , and hence we estimate the number of interacting ERO companions per ERO as $\frac{10.01 \pm 3.09}{200} = 0.050 \pm 0.015$.

This calculation was repeated using only the 157 EROs with $K_s < 21.25$ EROs (to avoid incompleteness effects); this found 16 ERO pairs compared to 7.43 ± 2.86 expected (Figure 14b), the correction at < 1 arcsec is $\frac{5}{1.47} \times 0.25 = 0.85$ and hence we estimate the number of interacting ERO companions per ERO as $\frac{9.42 \pm 2.86}{157} = 0.060 \pm 0.018$.

These estimates are a little higher than the Patton et

al. (2002) estimate for optically-selected galaxies at $z = 0.3$, but if this evolves at $(1+z)^{2.3}$, it would reach 0.06 at $z = 0.71$. Hence we tentatively conclude that if this method is reasonably valid the incidence of interacting/merging pairs amongst EROs does not seem to significantly higher than for a full optically-selected sample of galaxies at similar redshifts ($z \sim 0.9(2)$).

8 CORRELATION OF EROs WITH X-RAY SOURCES

The CDFS was surveyed with Chandra in two passbands, $0.5(2.0$ keV (‘Soft’) and $2(10$ keV (‘Hard’), reaching (in a total of 942 ksec exposure time) respective source-detection limits of 5.5×10^{-17} and 4.5×10^{-16} erg $s^{-1} cm^{-2}$ (which are 12 and 15 counts Mpc^{-1}). Giacconi et al. (2002) catalog the X-ray sources, numbering a total of 346 detections in the Soft (307) and/or Hard (251) bands, of which 73 are in the area of our Isaac data.

For each source, an X-ray hardness ratio HR is given as $\frac{H-S}{H+S}$ where H and S are the photon counts in the Hard and Soft bands, and can take any value from $HR = -1$ (detected only in Soft band) to $HR = +1$ (detected only in Hard). The total X-ray flux and HR can help to classify the source (Alexander et al. 2002; Vignali et al. 2003) as an AGN, starburst or elliptical galaxy. A flat spectrum (photon index $= 1.0$) is $HR \sim 0.11$. Unobscured AGN and starburst galaxies have $f_{\nu} \propto \nu^{-1}$ ($= 2.0$) SEDs, which is $HR \sim 0.35$, with the starbursts having lower X-ray luminosities, $L_X \sim 10^{42} h^2$ erg s^{-1} , and hence at $z > 1$, fluxes $F(0.5-10$ keV) $\sim 4 \times 10^{-16}$ erg $s^{-1} cm^{-2}$. Passive ellipticals, containing hot gas, have a similarly soft HR and an even lower L_X . Obscured AGN will have a harder HR, depending on the absorption column, N_H and redshift.

We cross-correlate these 73 X-ray sources with the ERO sample with the two aims of (i) identifying which EROs are also X-ray sources and (ii) of investigating whether there is any association between EROs and X-ray sources at non-zero separations.

8.1 Calculating the cross-correlation

The high spatial resolution (FWHM ~ 0.7 arcsec) of Chandra provides source positions with sufficient accuracy for easy identification with individual faint galaxies. Firstly, we positionally matched Chandra sources with the K_s -band detections on the Isaac mosaic, and found 68 of these to have probable K_s counterparts (within 2.5 arcsec). To better optimize the cross-correlation, we fitted an astrometric transform between the X-ray RA and Dec coordinates of (65 of) these sources and the pixel positions of their K_s -band counterparts, and using this transform (which had an rms error of only 0.44 arcsec), converted all Chandra source positions to pixel co-ordinates on the K_s image.

The 73 Chandra sources were then cross-correlated with the 200 $I - K_s > 3.75$ EROs, by the same methods as in Section 6.1, evaluating

$$!_{xe}(i) = \frac{N_{xe}(i) N_e}{N_{xr}(i) N_r} - 1$$

where $N_{xe}(i)$ is the total number of Chandra-ERO pairs

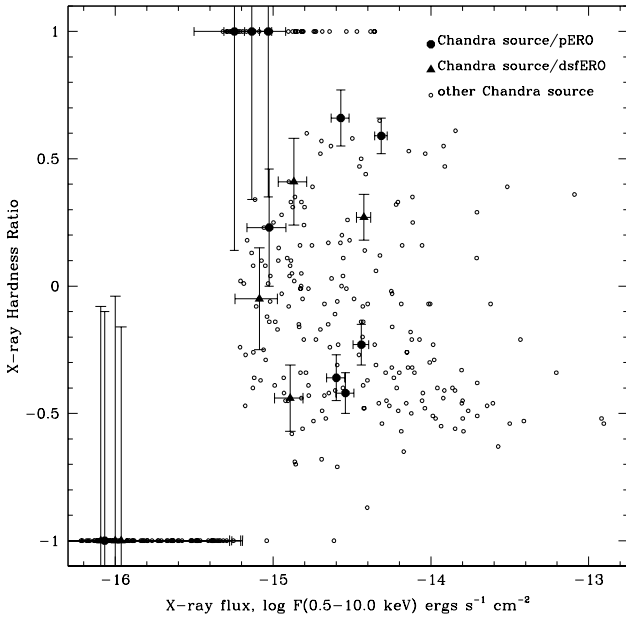


Figure 15. X-ray flux at 0.5{10.0 keV, against hardness ratio (HR), for EROs (large symbols) and other X-ray sources detected with Chandra on the CDFS.

(centering on the Chandra sources) in the $\Delta\theta$ interval of angular separation, $N_{\text{cr}}(\Delta\theta)$ the number of Chandra{random pairs, N_{e} the number of EROs and N_{r} the number of random points (50000 here).

8.2 X-ray detected EROs

Firstly, EROs were identified directly with Chandra sources where the K_s band and X-ray positions coincide within 2.0 arcsec, in each case checking by eye that the correct counterpart is selected. A total of 17 direct matches were found. Hence 8.5 { 2.1 per cent of the K_s { 22.0 { $I_K > 3.75$ EROs are identified as X-ray detections, and 23.3 { 5.6 per cent of the Chandra sources as EROs. Table 4 gives details of these 17 objects. Of these EROs, $\frac{16}{17}$ have $I_K > 4.0$, and 10 are classed as pEROs and 7 as dsEROs, so the X-ray detected fractions amongst pEROs and dsEROs are very similar, 8.6 { 2.7 and 8.3 { 3.1 per cent.

Figure 15 plots total 0.5{10.0 keV flux (i.e. the sum of the 0.5{2.0 and 2.0{10.0 keV fluxes, assuming a zero flux for any band in which there is no detection) against HR, and can be compared directly with Figure 4 of Alexander et al. (2002) and Figure 2 of Vignali et al. (2003).

The non-ERO Chandra sources are spread widely over the $0.6 < \text{HR} < 0.6$ range, consistent with $0 < z < 4$ AGN with wide range of obscuring column, from $\log N_{\text{H}} < 10^{22}$ to $10^{23.5} \text{ cm}^{-2}$ (Barger et al. 2002). At $\text{HR} \approx 0.4$, their distribution shows a horizontal ‘spur’ towards brighter fluxes, presumably comprised of the X-ray luminous, unobscured QSOs.

Of ERO X-ray sources, 10 (6 pEROs and 4 dsEROs) are spread over the same HR range, with fluxes, $F(0.5\{10.0 \text{ keV}) > 6 \times 10^{16} \text{ ergs s}^{-1} \text{ cm}^{-2}$, sufficient to indicate

AGN. These AGN must be obscured to some degree for the galaxies to exhibit ERO colours. The HR range implies $N_{\text{H}} \approx 10^{22} \{ 10^{23.5} \text{ cm}^{-2}$, and the pERO/dsERO mixture varied star-formation histories in their host galaxies.

A further 3 pEROs are detected in the Hard band only. Their Hard fluxes (in combination with the Soft band upper limit) indicate that they have $\text{HR} > 0.1$ and host obscured AGN. Finally, 3 dsEROs and one pERO are detected in the Soft band only, with the Soft fluxes (combined with the Hard band upper limit) indicating $\text{HR} < 0$. These relatively faint sources may be non-AGN, e.g. three starbursts and a giant elliptical, although weak AGN are not excluded. On the Isaac images two of these dsEROs look like interacting galaxies but the third is point-like and the pERO appears small and faint. The forthcoming HST Advanced Camera imaging may clarify their galaxy/AGN nature.

These results can be compared with, firstly, Alexander et al. (2002), who found that a 1M Sec Chandra survey of the CDFN detected 6 of 29 brighter $H_K^0 < 20.4$ EROs ($I_K > 4.0$) and 1 of 9 $K < 22$ EROs. Of a total of 13 X-ray detected EROs, nine were detectable in the Hard band (with $\text{HR} \approx 0.33$ to 0.6), implying they are obscured AGN with the same range of N_{H} and z as their CDFS counterparts, while the four detected only in the Soft band were thought to be an elliptical and three dusty starbursts.

Vignali et al. (2003) repeated this cross-correlation on the same field, with the addition of more Chandra data bringing the exposure time to 2M sec. Some additional EROs were detected, bringing the numbers to 10 of 29 $H_K^0 < 20.4$ and 3 of 9 $K < 22$ EROs.

Clearly, these results and ours are similar and a consistent picture of the X-ray properties of EROs is emerging from the CDFS and CDFN.

8.3 The X-ray{ERO Correlation at $\Delta\theta > 0$

We find evidence of a cross-correlation between Chandra sources and EROs at non-zero separations.

Figure 16a shows the Chandra source/ERO cross-correlation, at a $K_s = 21.25$ limit for the EROs (where incompleteness should be small). It remains positive at 2 { 20 arcsec, where any signal must be produced by clustering between separate objects. A function $\mathcal{A}(\Delta\theta) \propto \exp(-\Delta\theta/12.24)$ fitted at $2.0 < \Delta\theta < 20$ arcsec, gave an amplitude at one degree of $30.2 \pm 13.4 \times 10^{-4}$ (a ≈ 2.25 signal), which is approximately half the ERO $\mathcal{A}(\Delta\theta)$ amplitude.

These results can be considered together with the Almaini et al. (2002) cross-correlation of Chandra and SCUBA sources. This found few coincidences between the two { Chandra detected only 1 of 17 SCUBA sources { but a significant cross-correlation at $5 < \Delta\theta < 100$ arcsec separations, where the mean cross-correlation function was ≈ 1.6 .

Our Chandra{ERO correlation differs from this in the greater number of direct coincidences, and some of our signal might be simply due to the fact that some Chandra sources are also EROs, and EROs are strongly clustered amongst themselves. However, if we exclude the 17 Chandra sources identified as EROs and cross-correlate only the other 56 with the EROs, the cross-correlation falls to zero at $\Delta\theta < 2$ arcsec (as expected), but it is little changed at $\Delta\theta > 2$ arcsec, where the best-fitting amplitude is $39.9 \pm 16.8 \times 10^{-4}$. This indicates that that faint X-ray sources (AGN and starbursts)

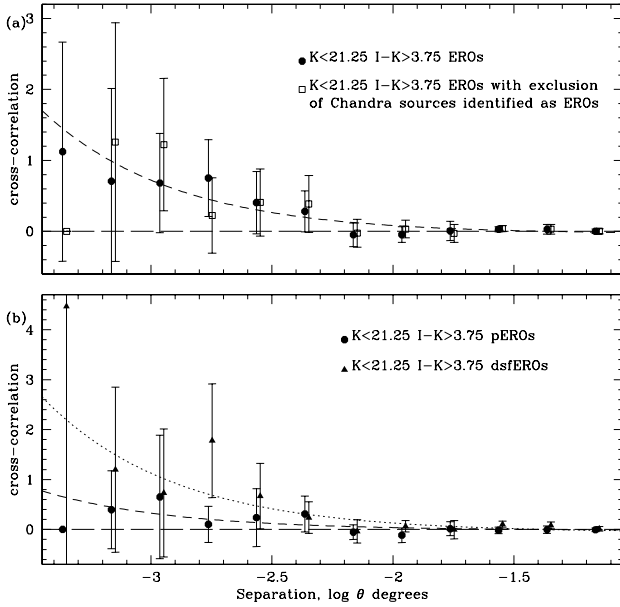


Figure 16. (a) Cross-correlation function, at non-zero separations, between Chandra sources (73) and $K < 21.25$ $I - K > 3.75$ EROs (157) on the Isaac Infrared area of the CDFS, also shown with the exclusion of Chandra sources identified as EROs (leaving 56) (b) Cross-correlation function between Chandra sources (73) and $K < 21.25$ $I - K > 3.75$ EROs separated by colours into 'pERO' (96) and 'dsfERO' (61) subsamples.

in general (i.e. not just the very reddened ones) at $z \sim 1$ tend to be clustered with EROs.

Secondly, it is possible that gravitational lensing of the Chandra sources by the background sub-mm sources accounts for much of their cross-correlation (Maini et al. 2003b, and in prep.), especially as their $N(z)$ appear to be offset with the former peaked at only $z \sim 1$ (Hornscheimer et al. 2001), whereas Ivison et al. (2002) estimate $z_{\text{median}} \sim 2.0$ for the SCUBA sources in ELAIS N2.

However, for any type of source the effect of lensing on the observed surface density depends on its number count slope; for a power-law $\frac{dN}{dm} = \dots$ the cumulative count to magnitude is modified by a multiplicative factor $2.5^{\Delta m}$, where Δm is the lensing magnification (Maini et al. 2003b). The sub-mm number counts are extremely steep, $\Delta m \sim 1$, whereas the majority of the EROs are at $K_s > 19.25$ where we find $\Delta m \sim 0.16$. Lensing of $\Delta m \sim 1.25$ near a cluster would then enhance the probability of finding a SCUBA source by 40 per cent but reduce the number of EROs by 10 per cent. Furthermore, current data (e.g. Cimatti et al. 2002) place the peak of the ERO $N(z)$ EROs much to the bulk of Chandra sources than SCUBA sources appear to be, favouring physical association over lensing. Hence we interpret our results as indicating that faint Chandra sources and EROs do tend to be physically associated, i.e. they trace the same large-scale structures and overlap greatly in $N(z)$.

We also cross-correlated the 73 Chandra sources with the separate pERO and dsfERO subsamples (Figure 16b). At $z \sim 2.0$ the best-fit amplitudes are 13.7 ± 10.9 and $47.2 \pm 21.2 \times 10^{-4}$ respectively.

Hence (although very similar fractions of the pEROs and dsfEROs are X-ray detected) there is at least a marginal suggestion that dsfEROs may be more strongly clustered with X-ray source galaxies than are pEROs. However, more data are needed to confirm this. Secondly, it is notable that the Chandra source dsfEROs cross-correlation alone is of > 2 significance, implying that the latter must be clustered.

9 SUMMARY AND DISCUSSION

1. We identify a sample of 200 EROs, defined as $I - K_s > 3.75$, galaxies, to $K_s = 22$ on public ESO/GOODS data covering 50.4 arcmin^2 of the Chandra Deep Field South (CDFS). Of these, 163 satisfy a stricter colour selection of $I - K_s > 4.0$.

The number counts of the CDFS EROs are lower than predicted by a pure luminosity evolution (PLE) model for E/S0 galaxies, and attenuated at $K_s \sim 19.0$ (19.5, from ~ 0.66 to ~ 0.11 to ~ 0.16 to ~ 0.05). At $K_s > 20$, this attenuation takes the ERO counts below even a non-evolving model for E/S0s, confirming that the comoving number density of EROs (and not only their mass or luminosity) is reduced compared to that of local E/S0 galaxies.

The ERO counts are well fitted by the 'merging and negative density evolution' (M-DE) model proposed in Paper I, in which a local luminosity function for E/S0 galaxies is evolved through a combination of (i) passive evolution, (ii) merging at a moderate, evolving rate based on an observational estimate (Patton et al. 2002), and (iii) a reduction with redshift in comoving number density, parameterized as R .

To $K_s = 21.5$ (the approximate completeness limit), the ERO counts were best-fit with $R \sim 0.50$ (± 0.06), which is a 43 (62) per cent reduction in the comoving number density of red/passive galaxies from $z = 0$ to $z = 1$ (2). This implies some $\frac{1}{3}$ fraction of the present day comoving number density of E/S0 galaxies formed at $z > 3$ and the remainder from mergers and interactions of bluer galaxies over all intermediate redshifts, so that the passive-galaxy population continually increases with time.

However, it must be noted that in addition to the K_s (Isaac) data incompleteness at $K_s > 21.5$, our ERO counts suffer a further source of uncertainty beyond $K_s \sim 21$ from the fact that the available I-band (FORS1) data are ~ 1 mag less deep, relative to the JHK_s data, than would have been optimal. The result of this is that the majority of our fainter EROs are below the detection threshold in I, and, although we can still estimate their $I - K$ colours in apertures, these will have large statistical errors. Hence we intend to check the fainter ERO counts, and probably achieve some improvement in accuracy, by reselecting the sample using the forthcoming HST Advanced Camera data for the I-band.

2. We investigate the clustering of the CDFS EROs and detect a > 3 signal in their angular correlation function, $\xi(\theta)$. We combine their best-fit $\xi(\theta)$ amplitudes with those from previous studies of ERO clustering (Paper I; Daddi et al. 2000; Firth et al. 2002), and interpret using Limber's formula. Assuming our M-DE model $N(z)$, the $\xi(\theta)$ scaling of EROs at $K = 18$ (22 limit) is well-fitted with comoving

($\beta = 1.2$) clustering and correlation radius $r_0 = 11(12 h^{-1} \text{ Mpc})$, or stable clustering ($\beta = 0$) and $r_0 = 20(21 h^{-1} \text{ Mpc})$.

As in previous studies, the EROs are significantly more clustered a full K -limited sample of galaxies, which has an β (β) consistent with the locally measured $r_0 = 5.85 h^{-1} \text{ Mpc}$ and $\beta = 0.4$. EROs are even more clustered than the $r_0 = 8 h^{-1} \text{ Mpc}$ of the local giant ($L > L^*$) ellipticals, indicating strong clustering evolution if they are direct progenitors of the E/SOs. This could be part of the same process as their evolution if the oldest EROs formed in the densest regions of the early Universe, and so are highly biased and strongly clustered, while the younger EROs added at lower redshift form from less strongly clustered disk galaxies and progressively dilute the red-galaxy (r) down to its present-day value. This would also account for a preliminary COMBO 17' finding (Phleps and Meisenheimer 2002) of strong clustering evolution, $\beta = 1.35 \pm 0.24$, for E(Sb) type galaxies over the $0 < z < 1$ range.

Daddi et al. (2002) found a large difference in the estimated r_0 of pEROs and dsfEROs at $z \sim 1$, although on the basis of a small sample, and in redshift space only. We have not been able to either confirm or exclude this, as the large error bar in our estimate of the dsfERO β (β) would allow both zero and pERO-like clustering. However, the cross-correlation we find between Chandra sources and dsfEROs (see Section 8.3) at $\sim 2(20 \text{ arcsec})$ separations would require there must be some clustering amongst the latter.

The rate of ERO clustering evolution and the question of pERO vs. dsfERO clustering should both be determined soon as, (i) the forthcoming HST Advanced Camera data will provide further passbands, enabling estimation of photometric redshifts and hence of the clustering evolution with redshift (as in e.g. Amoutsos et al. 2002), (ii) the extension of the GOODS/ESO survey over the whole CDFS will provide a much larger sample, and (iii) our planned spectroscopic survey will allow investigation of clustering in three dimensions, and (iv) forthcoming measurements of the clustering of SCUBA sources (Percival et al. 2003) will provide an essential high- z point of comparison.

3. There is an overdensity of EROs centered on the Chandra X-ray source XID 58, a $K_s = 20.94$ galaxy and itself an ERO, at R.A. $3^{\text{h}} 32^{\text{m}} 11.85^{\text{s}}$, Dec $-27:46:29.14$. Within 20 arcsec of this object, we find 11 $K_s < 22$ EROs, compared to 1.39 expected by chance, and furthermore 7 of these (including the X-ray source) have similar IJH K_s colours consistent with passive galaxies at $z \sim 1.5$ (and two of the other 4 might be dsfEROs at the same redshift). Hence there is evidence of a real cluster.

This cluster lacks central concentration in that the central galaxy (the X-ray source) is one of the optically fainter probable members and the brightest EROs are scattered over the cluster area. This might indicate the cluster is still forming. There is also no detection with Chandra of any diffuse X-ray emission from hot gas in the cluster, although this might be typical at $z \sim 1.5$ in view of the rapid negative evolution with redshift seen in the X-ray luminosity function of clusters (e.g. Henry 2003).

The point-source X-ray emission from the central elliptical indicates it to host an AGN, despite its modest optical luminosity ($M_R = 22.05$), which implies a sub- L^* mass. This contrasts with the $L > L^*$ masses of local quasar hosts,

but can be accounted for by the increase in black-hole fueling rates at these redshifts, which allows for host galaxies at least a factor 2 less massive (Kukula et al. 2001). We note that Willott et al. (2002) found an L^* - L^* passive ERO in ELAIS N2 (object N228) with a very similar X-ray to K -band flux ratio.

With HST imaging and spectroscopy, this and other high- z clusters will provide useful samples of declining luminosity EROs at a common redshift, enabling a comparison of properties such as radial profiles, estimated stellar ages and metallicities.

4. We investigate the numbers of close (i.e. probably interacting) pairs of EROs, using the method of Woods, Fahlman and Richer (1995) with the same $P = 0.05$ selection, and estimate the number of interacting ERO companions per ERO as 0.05 ± 0.015 to $K = 22$, or 0.06 ± 0.018 to the more complete $K = 21.25$ limit. By comparison, Patton et al. (1992) estimated that amongst normal, optically-selected galaxies, there were 0.0321 ± 0.007 interacting companions per galaxy at $z \sim 0.3$ with evolution as $(1+z)^{2.13}$ out to $z \sim 1$. Hence the pair fraction we estimate for EROs is consistent with that expected for optically-selected galaxies at $z \sim 0.7$, i.e. the ERO redshifts.

This contrasts markedly with the radio-selected faint galaxies, which at Jy fluxes consist primarily of strong starbursts. Some 30(60 per cent) of these are visibly interacting (Windhorst et al. 1995; Roche, Lowenthal and Koo 2002a), reflecting the importance of tidal triggering in producing the highest star formation rates.

Although, there is no obvious reason for pEROs to be preferentially associated with interactions, an enhanced merger fraction would be expected for dsfEROs, if these are (as we hypothesise), undergoing a disk-to-elliptical transformation. However, (i) some radio-selected faint galaxies appear unpaired and quite normal at ground-based resolution but are revealed by HST observations to have post-interaction features such as 'starburst rings' (Roche, Lowenthal and Koo 2002b); (ii) the high dsfEROs/pERO ratio (see Paper I) suggests the mean lifetime of the dsfERO stage is much longer ($\sim 1 \text{ Gyr}$) than the timescales of merger-triggered starbursts ($\sim 0.1 \text{ Gyr}$), and hence that many must be in post-burst stages; (iii) simulations indicate the most dust-reddened mergers are those occurring in a retrograde-retrograde geometry (Bekki and Shioya 2000), which also tend to starburst at a late stage of merging and lack obvious tidal tails.

On this basis, starburst-mergers would be most likely to be selected as dsfEROs in late, post-coalescence or post-merger stages, when they would be counted as single galaxies rather than as pairs. To investigate this possibility, we plan to use the forthcoming HST Advanced Camera data to look for more subtle post-interaction features.

5. We find 17 coincidences between the 73 Chandra X-ray sources and the 200 EROs ($K_s \geq 22$ I $K_s > 3.75$) in our data area, which means that 8.5 ± 2.1 per cent of the EROs are X-ray detected and 23.3 ± 5.6 per cent of the Chandra sources are EROs. The fractions of pEROs and dsfEROs which are X-ray detected are similar, which would reflect the diversity of emission and absorption line galaxies amongst faint AGN hosts (Barger et al. 2002).

Of these 17 sources, 13 are detected in the Hard band,

with fluxes sufficient to require the presence of AGN. The wide range of their hardness ratios is consistent with AGN with a wide range of obscuring column, $N_{\text{H}} \sim 10^{22} - 10^{23.5} \text{ cm}^{-2}$. Four EROs were detected only in the Soft band (3 dsfEROs and one pERO) and may be non-AGN galaxies i.e. ellipticals and starbursts. These results are very similar to those of Alexander et al. (2002) for EROs on the CFN. The results of Vignali et al. (2003) suggest that a further 10 per cent of the EROs would be revealed as faint X-ray sources by increasing the exposure from 942 ksec to 2 Msec, which would bring the fraction of EROs hosting obscured AGN to the same (20 per cent) as suggested by the VLA observations of Paper I.

We also make the interesting discovery of a cross-correlation between Chandra sources and EROs at non-zero (~ 20 arcsec) separations, with an amplitude about half that of the EROs. This cross-correlation is not significantly reduced when the 17 Chandra sources coincident with EROs are excluded, which implies that EROs are clustered with AGN and starbursts in general (i.e. not only with those that are heavily reddened) at $z \sim 1.2$. There is an admittedly marginal (sub-2 σ) indication that the Chandra sources are more correlated at > 2 arcsec with the dsfEROs than the pEROs.

A correlation between pEROs and AGN would be expected if pEROs form from SCUBA-source type starbursts via a QSO phase (see Paper I), so would tend to occupy the same high-density environments as active QSOs. However, pEROs will by definition have long stellar ages, ~ 3 Gyr (Nolan et al. 2003), and this might introduce a tendency for pEROs to inhabit dynamically older clusters than 'average' QSOs.

Some AGN activity is associated with late-stage or recent starbursting, whether in the formation of ellipticals (Archibald et al. 2002), following gas-rich mergers, as in local ULIRGs (e.g. Tacconi et al. 2002), or in the starburst 'jets' of radio galaxies (e.g. Best et al. 1997). Secondly, some high-redshift AGN, e.g. the radio galaxy 53W002, are hosted by passive galaxies but surrounded by starbursts (e.g. Pascarelle et al. 1998). If Chandra sources are confirmed as being more correlated with the dsfEROs, this could be due to the dsfEROs and AGN being associated in the evolutionary stage as well as in the density of environment, i.e. both preferring 'young' cluster regions with a lot of gas and a lot of current star formation.

We plan to investigate further the cross-correlations and environments of faint X-ray sources, pEROs and dsfEROs, in three dimensions using spectroscopy.

Acknowledgements

This paper is based on observations with the ANTU Very Large Telescope, operated by the European Southern Observatory at Cerro Paranal, Chile, and forming part of the publically available ESO/GOODS dataset.

NR acknowledges the support of a PPARC Research Associateship. OA acknowledges the support of a Royal Society Research Fellowship. JSD acknowledges the support of a PPARC Senior Fellowship.

REFERENCES

- Alexander D. M., Vignali C., Bauer F. E., Brandt W. N., Homsher A. E., Gamire G. P., Schneider D. P., 2002, *AJ*, 123, 1149.
- Imai O., et al., 2003a, *MNRAS*, 338, 303.
- Imai O., 2003b, 'X-ray Surveys in the light of new observatories', workshop proceedings (4-6 September 2002, Santander, Spain), in press. (astro-ph/0211353)
- Archibald E. N., Dunlop J. S., Jimenez R., Friis A., McLure R. J., Hughes D. H., 2002, *MNRAS*, 336, 353.
- Aumouts S., et al., 2002, *MNRAS*, 329, 355.
- Barger A., Cowie L., Brandt W. N., Capak P., Gamire G. P., Homsher A. E., Steen A. T., Wehner E. H., 2002, *AJ*, 124, 1839.
- Baugh C. M., Gardner J. P., Frenk C. S., Sharples R. M., 1996, *MNRAS*, 283, L15.
- Bekki K., Shioya Y., 2000, *ApJ*, 542, 201.
- Bertin E., Aumouts S., 1996, *A&S*, 117, 393.
- Best P. N., Longair M. S., Rottgering J., 1997, *MNRAS*, 292, 758.
- Cabanac A., de Lapparent V., Hickson P., 2000, *A&A*, 364, 349.
- Comati A., et al., 2002a, *A&A*, 381, 68.
- Daddi E., Comati A., Pozzetti L., Hoekstra H., Rottgering J., Renzini A., Zamorani G., Mannucci F., 2000, *A&A*, 361, 535.
- Daddi E., et al., 2002, *A&A*, 384, 1.
- Dickinson M., Giavalisco M., 2002, 'The Mass of Galaxies at Low and High Redshift', ESO/USM Workshop, (Venice, Italy, October 2001), eds. R. Bender and A. Renzini. (astro-ph/0204201)
- Firth A. E., et al., 2002, *MNRAS*, 332, 617.
- Giacconi R., et al., 2002, *ApJS*, 139, 369.
- Giavalisco M., Dickinson M., 2001, *ApJ*, 550, 177.
- Guzzo L., Strauss M., Fisher K., Giovanelli R., Haynes M., 1997, *ApJ*, 489, 37.
- Homsher et al., 1998, *ApJ*, 554, 742.
- Henry J. P., 2003, 'Matter and Energy in Clusters of Galaxies', conference proceedings, in press. (astro-ph/0207148).
- Iverson R. J., et al., 2002, *MNRAS*, 337, 1.
- Kochanek C., et al., 2001, *ApJ*, 560, 566.
- Kukula M. J., Dunlop J. S., McLure R. J., Miller L., Percival W., Baum S. A., O'Dea C. P., 2001, *MNRAS*, 326, 1533.
- Imai O., 2003, PhD Thesis.
- Mannucci F., Pozzetti L., Thompson D., Oliva E., Baia C., Comoretto G., Gennari S., Lisif., 2002, *MNRAS*, 329, 57.
- McCracken H., Shanks T., Motalleb N., Fong R., Campos A., 2000, *MNRAS*, 318, 913.
- Moustakas L., Davis M., Graham J., Silk J., Peterson B., Yoshii Y., *ApJ*, 475, 445.
- Nolan L., Dunlop J., Jimenez R., Heavens A., 2003, *MNRAS*, in press (astro-ph/0103450).
- Pascarelle S. M., Windhorst R. A., Keel W. C., 1998, *AJ*, 116, 2659.
- Patton D., et al., 2002, *ApJ*, 565, 208.
- Pen Ue-Li, 1999, *ApJS*, 120, 49.
- Percival W. J., Scott D., Peacock J. A., Dunlop J. S., 2003, *MNRAS*, in press. (astro-ph/0211599).
- Phleps S., Meisenheimer K., 2002, 'The Evolution of Galaxies III. From Simple Approaches to Self-Consistent Models', conference proceedings (Kiel, Germany, July 2002). (astro-ph/0209294).
- Pozzetti L., Mannucci F., 2000, *MNRAS*, 317, 17.
- Roche N., Imai O., Dunlop J., Iverson R. J., Willott C. J., 2002, *MNRAS* 337, 1282. (Paper I)
- Roche N., Lowenthal J., Koop D., 2002a, *MNRAS*, 330, 307.
- Roche N., Lowenthal J., Koop D., 2002b, *MNRAS*, 337, 840.
- Roche, N., Eales S., Hippelein H., Willott, C. J., 1999, *MNRAS*, 306, 538.
- Roche, N., Eales S., Hippelein H., 1998, *MNRAS*, 295, 946.
- Saracco P., Giavalisco E., Cristiani S., D'Odorico S., Fontana A.,

- Iovino A., Poli F., Vanzella E., 2001, *A & A*, 375, 2001.
- Saracco P., et al., 2003, *A & A*, in press. (astro-ph/0211394).
- Scott S., et al., 2002, *MNRAS*, 331, 817.
- Spergel D N., et al., 2003, *ApJ*, in press. (astro-ph/0302209).
- Szokoly G., et al., 2003, *ApJ*, submitted.
- Tacconi L.J., Genzel R., Lutz D., Rigopoulou D., Baker A.J., Iserlohe C., Tecza M., 2002, *ApJ*, 580, 73.
- Vignali C., Alexander D.M., Bauer F.E., Brandt W.N., Homschermeyer A.E., Gammire G.P., Schneider D.P., 2003. 'Inflows, Outflows and Reprocessing around black holes', proceedings of 5th Italian AGN Meeting, in press. (astro-ph/0209415).
- Woods D., Fahlman G., Richer H., 1995, 1995, *ApJ*, 454, 32.
- Willott C.J., et al., 2003, *MNRAS*, in press. (astro-ph/0210248)
- Windhorst R.A., Fomalont E.B., Kellermann K.I., Partridge R.B., Richards E., Franklin B.E., Pascarella S.M., Grieths R.E., 1995, *Nature*, 375, 471.